A NEAR-INFRARED ANALYSIS OF THE SUBMILLIMETER BACKGROUND AND THE COSMIC STAR-FORMATION HISTORY

W.-H. Wang,[1] L. L. Cowie,[1] and A. J. Barger[2,3,1]

ABSTRACT

We use new deep near-infrared (NIR) and mid-infrared (MIR) observations to analyze the 850 μm image of the Great Observatories Origins Deep Survey-North region around the Hubble Deep Field-North. We show that much of the submillimeter background at this wavelength is picked out by sources with $H(AB)$ or 3.6 μm$(AB) < 23.25$ (1.8 μJy). These sources contribute an 850 μm background of 24 ± 2 Jy deg^{-2}. This is a much higher fraction of the measured background $(31 - 45$ Jy deg$^{-2})$ than is found with current 20 cm or 24 μm samples. Roughly one-half of these NIR-selected sources have spectroscopic identifications, and we can assign robust photometric redshifts to nearly all of the remaining sources using their UV to MIR spectral energy distributions. We use the redshift and spectral type information to show that a large fraction of the 850 μm background light comes from sources with $z = 0 - 1.5$ and that the sources responsible have intermediate spectral types. Neither the elliptical galaxies, which have no star formation, nor the bluest galaxies, which have little dust, contribute a significant amount of 850 μm light, despite the fact that together they comprise approximately half of the galaxies in the sample. The galaxies with intermediate spectral types have a mean flux of 0.40 ± 0.03 mJy at 850 μm and 9.1 ± 0.3 μJy at 20 cm.

The redshift distribution of the NIR-selected 850 μm light lies well below that of the much smaller amount of light traced by the more luminous, radio-selected submillimeter sources. We therefore require a revised star-formation history with a lower star-formation rate at high redshifts. We use a stacking analysis of the 20 cm light in the NIR sample to show that the star-formation history of the total 850 μm sample is relatively flat down to $z \sim 1$ and that half of the total star formation occurs at redshifts $z < 1.4$.

Subject headings: cosmology: observations — galaxies: evolution — galaxies: formation — galaxies : starburst — infrared: galaxies — submillimeter

1. INTRODUCTION

The integrated extragalactic background light (EBL) is a measure of the history of the luminous energy production of the universe from both star formation and active galactic nuclei (AGNs). Directly emitted light is seen in the UV and optical, whereas dust reradiated energy appears in the far-infrared (FIR) and submillimeter. *COBE* obtained detailed measurements of the EBL at FIR and submillimeter wavelengths (e.g., Puget et al. 1996; Fixsen et al. 1998), showing that the total radiated emission reprocessed by dust in the FIR/submillimeter is comparable to the total measured optical EBL. However, to proceed further, we also need to know the redshift distribution of the sources contributing to the submillimeter background, and this information has been extremely difficult to obtain.

In the last decade, the submillimeter/millimeter EBL has been resolved into discrete sources by deep surveys with the Submillimeter Common-User Bolometer Array (SCUBA) on the 15 m James Clerk Maxwell Telescope (JCMT) and with the Max-Plank Millimeter Bolometer array on the 30 m IRAM telescope. Blank-field surveys have resolved sources in the $2 - 20$ mJy range that account for $\sim 20 - 30\%$ of the

850 μm EBL (e.g., Barger et al. 1998; Hughes et al. 1998; Barger, Cowie, & Sanders 1999a; Eales et al. 1999, 2000, 2003; Bertoldi et al. 2000; Scott et al. 2002; Webb et al. 2003; Borys et al. 2003; Wang, Cowie, & Barger 2004). With the help of strong lensing, surveys in cluster fields have resolved sources over the $0.3 - 2$ mJy range that account for a further $45 - 65\%$ of the 850 μm EBL (Smail, Ivison, & Blain 1997; Chapman et al. 2002; Cowie, Barger, & Kneib 2002; Knudsen et al. 2005). Together these surveys provide a nearly complete resolution of the background at 850 μm. The "typical" source contributing to the 850 μm EBL has a mean flux of about 0.9 mJy and a median flux of about 0.6 mJy (Cowie, Barger, & Kneib 2002).

However, the redshift follow-up of the submillimeter sources has been very slow. Because of the large beam size $(15'')$ of SCUBA and the optically-faint nature of the dusty sources, identifying the optical and near-infrared (NIR) counterparts to the submillimeter sources is time consuming (e.g., Barger et al. 1999b; Ivison et al. 2000). To date, the most successful identifications of the submillimeter sources rely on the empirical correlation between the nonthermal radio emission and the thermal dust emission (e.g., Condon 1992). Once the radio counterparts to the submillimeter sources are detected by radio interferometers, the redshifts of the sources can be crudely estimated using the radio-to-submillimeter flux ratios (Carilli & Yun 1999; Barger, Cowie, & Richards 2000; Hughes et al. 2002; Ivison et al. 2002; Chapman et al.

---

[1] Institute for Astronomy, University of Hawaii, 2680 Woodlawn Drive, Honolulu, HI 96822

[2] Department of Astronomy, University of Wisconsin-Madison, 475 North Charter Street, Madison, WI 53706

[3] Department of Physics and Astronomy, University of Hawaii, 2505 Correa Road, Honolulu, HI 96822

2003b) or accurately measured with optical spectroscopy (Chapman et al. 2003a, 2005). The radio-identified sources are mostly bright ($\gg$ 2 mJy) submillimeter sources at $z = 1.5 - 3.5$, with properties similar to the local ultraluminous infrared galaxies (ULIRGs; $L_{IR} > 10^{12} \, L_\odot$, where L_{IR} is the $8 - 1000 \, \mu$m infrared luminosity; see, e.g., Sanders & Mirabel 1996). We note, however, that because of the K-correction and the sensitivity limit in the radio, only $\sim 60\%$ of the bright submillimeter sources are identified in the radio (Barger, Cowie, & Richards 2000). It is not known whether the remaining 40% are at higher redshifts that simply cannot be reached by current radio telescopes.

Importantly, however, the properties and redshift distribution of the faint submillimeter sources that dominate the submillimeter EBL remain essentially unknown. The absence of any redshift information for more than 90% of the 850 μm EBL represents a formidable uncertainty in determining the star-formation history, and this is what we aim to resolve in the present paper.

Like the radio emission, the mid-infrared (MIR) emission at $\gtrsim 5 \, \mu$m could serve as another proxy to the submillimeter emission, since it also comes from dust. The MIR window has been opened by the Infrared Array Camera (IRAC, Fazio et al. 2004) and the Multiband Imaging Photometer for *Spitzer* (MIPS, Rieke et al. 2004) on the *Spitzer Space Telescope* (e.g., Huang et al. 2004; Serjeant et al. 2004; Ivison et al. 2004; Egami et al. 2004). MIPS should be sensitive to $z \lesssim 1$ galaxies with infrared luminosities similar to local normal galaxies ($L_{IR} \sim 10^{10} \, L_\odot$, corresponding to ~ 0.1 mJy at 850 μm) and to $z \lesssim 3.5$ ULIRGs (i.e., typical of the bright submillimeter sources). Thus, MIPS should be able to detect the radio-identified submillimeter sources at $z \lesssim 3.5$ and to provide a large sample of faint sources that are beyond the confusion limit of current submillimeter telescopes (e.g., Chary et al. 2004). However, as we shall show in this paper, even the extraordinarily deep MIPS data of the Great Observatories Origins Deep Survey-North (GOODS-N) *Spitzer* Legacy Science Program in the Hubble Deep Field-North (HDF-N) region does not substantially identify the 850 μm EBL.

Remarkably, however, the combination of a J or H-band sample (selected from images obtained with the new generation of ground-based, wide-field NIR cameras) and the IRAC 3.6 μm sample does identify much of the 850 μm EBL. We show this using the H-band image of the GOODS-N region obtained by Trouille et al. (2006). This result makes sense if the bulk of the sources contributing to the 850 μm EBL are actually at lower redshifts and luminosities than those identified at the brighter submillimeter fluxes. Such sources have strong rest-frame optical/NIR counterparts that are picked up in the NIR sample. We utilize the spectroscopic and photometric redshift information on our NIR sample to confirm this result. We find that more than half of the 850 μm EBL arises in sources with $z < 1.5$ and that the sources that are responsible have intermediate spectral types. Neither the elliptical galaxies, which have no star formation, nor the bluest galaxies, which have little dust, contribute substantially to the 850 μm EBL, despite the fact that together they comprise approximately half of the sample.

This result has profound implications for our under-

standing of the star-formation history, lowering previous estimates of the high-redshift star formation rate densities by factors of at least two. We analyze the star-formation history of our NIR sample using a 20 cm stacking analysis and compare this with the maximum star formation rate density at higher redshifts obtained directly from the submillimeter light. Together these show that the total star formation rate density peaks at a redshift at or just below one and is roughly flat at higher redshifts.

The paper is organized as follows. The submillimeter, NIR, MIR, optical, radio, and X-ray data are described in §2. The spectroscopic and photometric redshifts are discussed in §3. The use of the NIR, MIR, and radio populations to identify the submillimeter background is discussed in §4, and the 850 μm EBL identified by the NIR-sample is broken down by galaxy flux, color, spectral type, and redshift. The star-formation history is described in §5. Our main results are summarized in §6. Throughout the paper, we assume the WMAP cosmology: $H_0 = 71$ km s^{-1} Mpc^{-1}, $\Omega_M = 0.73$, and $\Omega_\Lambda = 0.27$ (Bennett et al. 2003).

2. THE DATA SAMPLES

2.1. *Submillimeter Data*

The GOODS-N submillimeter map of Wang, Cowie, & Barger (2004) is based on jiggle-map data taken primarily by our group using the SCUBA instrument on the JCMT. The data set has also been analyzed by Borys et al. (2003, 2004). The mosaicked submillimeter image has non-uniform $0.4-4$ mJy point-source sensitivity and covers 0.034 deg^2 (43% of the MIPS area) in the GOODS-N field. Forty-five 3σ and seventeen 4σ submillimeter sources are in the catalog of Wang, Cowie, & Barger (2004). We also used the submillimeter data to determine the 850 μm fluxes of the various samples. We measured the submillimeter fluxes and errors for these samples using optimal beam-weighted extractions (Wang, Cowie, & Barger 2004) throughout the area covered by our submillimeter image.

2.2. *Near-Infrared Data*

We carried out deep J and H-band imaging of the entire GOODS-N region using the Ultra-Low Background Camera (ULBCAM) on the University of Hawaii 2.2 m telescope during 2004 and 2005 (Trouille et al. 2006). ULBCAM consists of four 2k×2k HAWAII-2RG arrays (Loose et al. 2003) with a total $16' \times 16'$ field of view. The images were taken using a 13-point dither pattern with $\pm 30''$ and $\pm 60''$ dither steps in order to cover the chip gaps. The data were flattened using median sky flats from each dither pattern. The image distortion was corrected using the astrometry in the USNO-B1.0 catalog (Monet et al. 2003). The flattened, sky-subtracted, and warped images were combined to form the final mosaic with a $20' \times 20'$ area fully covering the GOODS-N region. The integration times at each pixel are 19 hours in J and 12.5 hours in H, respectively, and the 5σ sensitivities are 0.84 μJy and 2.06 μJy corresponding to 5σ AB magnitude limits of 24.1 and 23.1, respectively. A more extensive description of the data reduction and a detailed analysis may be found in Trouille et al. (2006).

We generated our source catalogs with the SExtractor package (Bertin & Arnouts 1996). Because the typical seeing was $0\rlap{.}''7$ and many of the sources appear extended in the images, we used auto aperture in SExtractor to ensure that the measured fluxes are close to the total fluxes. In our stacking analysis, we also consider a catalog of all $H(AB) < 24$ (roughly the 3σ limit) sources that lie within the submillimeter image. Although this catalog will include a small number of false detections ($\sim 1\%$, inferred from negative sources), this is not a significant issue for our stacking analysis, since these sources will not affect the signal and will only add a small amount to the noise.

2.3. IRAC Data

We used the GOODS-N *Spitzer* Legacy Science Program first, interim, and second data release products (DR1, DR1+, DR2; Dickinson et al. 2006). We combined the reduced DR1 and DR2 IRAC superdeep images, weighted by exposure time, to form 3.6, 4.5, 5.8, and 8.0 μm images that fully cover the GOODS-N area. We again generated the source catalogs in each band with the SExtractor package (Bertin & Arnouts 1996). We detected approximately 9800, 8500, 3600, and 3000 sources at $> 5\sigma$ at 3.6, 4.5, 5.8, and 8.0 μm, respectively. We measured the source fluxes with fixed apertures of $4\rlap{.}''8$ (3.6 and 4.5 μm) and $6''$ (5.8 and 8.0 μm). These apertures are approximately three times the $\sim 1\rlap{.}''7$ (3.6 μm) to $\sim 2''$ (8.0 μm) FWHM of the point spread function (PSF) and are a good compromise between the PSF size and the source separation. We applied aperture corrections from the IRAC in-flight PSFs (January 2004) to the measured fluxes. The aperture corrections we used are consistent with the ones published in the IRAC Data Handbook. The corrected IRAC fluxes should be reasonably close to the total fluxes of the sources, because the majority of the sources are point-like compared to the $\sim 2''$ IRAC PSF. The primary errors in the photometry are caused by the high density of sources, especially at 3.6 and 4.5 μm. In these two bands, the typical distance between sources is comparable to the PSF, and the maps are confusion-limited. Consequently, both the background estimate and the aperture photometry are highly subject to blending with nearby sources.

2.4. MIPS Data

At the longest MIR wavelengths, our sample consists of the MIPS 24 μm GOODS-N data. We directly used the DR1+ MIPS source list and the version 0.36 MIPS map provided by the *Spitzer* Legacy Program. The source catalog is flux-limited at 80 μJy and is a subset of a more extensive catalog (Chary et al. 2006). With the 0.065 deg^2 area coverage, the catalog contains 1199 24 μm sources and is $> 80\%$ complete at 80 μJy (Papovich et al. 2004). The source positions are based on sources detected in the deep IRAC images, and the fluxes are derived using PSF fitting. The flux limit and accuracy of this catalog are sufficient for our purposes, so we did not attempt to generate our own MIPS source catalog.

Nevertheless, because the DR+ MIPS source list is still preliminary, we verified the sources in the list using the MIPS map. We used a normalized MIPS PSF to convolve with the MIPS map and measured the 24 μm fluxes at the cataloged positions. These PSF-weighted fluxes are mostly consistent with the fluxes in the DR+ source list. However, there are a few sources at the edges of the MIPS map, where it is noisier, which have low-significance fluxes in our measurements. Seventeen of these sources have no obvious counterparts in the deep IRAC, NIR, and optical images. These sources are likely spurious. Thus, for our stacking analysis, we used a restricted area that was fully covered by the *Hubble Space Telescope* ACS GOODS-N observations, since this is where nearly all of our submillimeter coverage is. This fully avoids the edge problems described above.

A $-0\rlap{.}''38$ offset in declination was applied to the source positions to match the radio-frame astrometry (Richards 2000).

2.5. Optical Data

Capak et al. (2004) presented ground-based deep optical imaging of a very wide-field region around the HDF-N. The imaging covers the whole MIPS and IRAC area at U, B, V, R, I, z', and HK' bands. We searched for counterparts to the various samples in the catalog of Capak et al. (2004) using a $1''$ search radius. This search radius closely matches the PSF in the optical and the astrometry errors in the optical and MIR.

Where the images overlapped, we also cross-identified the various samples with the ACS GOODS-N catalog of Giavalisco et al. (2004).

2.6. Radio and X-ray Data

We used the 1.4 GHz catalog and image from Richards (2000), which contains sources to a flux limit of 40 μJy (5σ), to analyze the radio-selected submillimeter sample. We also used the radio data to determine the 20 cm fluxes of the various samples. We measured the 20 cm fluxes in $3''$ diameter apertures, adjusting the normalization to match the measured fluxes in the Richards (2000) catalog for the overlapping set of objects. We measured the noise level by determining the fluxes at a large number of random positions and then measuring the dispersion. The 1σ noise is 14 μJy, which is almost a factor of two higher than that measured by Richards (2000). This reflects the large aperture used. However, the noise distribution measured in this way is well fitted by a Gaussian, with an average zero flux level.

Finally, we used the *Chandra* Deep Field-North (CDF-N) 2 Ms catalog (Alexander et al. 2003) to determine the X-ray properties of the various samples and to identify sources that contain AGNs.

2.7. Data Summary

We summarize the flux limits of the various samples in Table 1. We also show the geometry of the various data sets schematically in Figure 1. The ground-based optical and NIR images cover the entire area shown. We mark the region with complete coverage from the ACS GOODS-N data with a rectangle and the submillimeter region with the contours. The overlap area constitutes our core area and covers 106 arcmin^2. Essentially all of this region lies within $8'$ *(circle)* of the X-ray and radio centers, where the X-ray and radio images have relatively uniform sensitivity. We denote the 4σ submillimeter sources with large open squares, the 20 cm sources

Band	Sensitivity Limit (μJy)	Telescope	Reference
MIPS 24 μm	80.0	*Spitzer*	a
IRAC 3.6 μm	0.327	*Spitzer*	a
IRAC 4.5 μm	0.411	*Spitzer*	a
IRAC 5.8 μm	2.27	*Spitzer*	a
IRAC 8.0 μm	2.15	*Spitzer*	a
U	0.052	KPNO 4 m	b
B	0.063	Subaru	b
V	0.069	Subaru	b
R	0.083	Subaru	b
I	0.209	Subaru	b
z'	0.251	Subaru	b
J	0.839	UH 2.2 m	c
H	2.06	UH 2.2 m	c

Note. — The MIPS 24 μm sample is flux-limited and complete at 80 μJy. The median 1σ sensitivity of the MIPS map is 6.4 μJy. For the rest of the bands, the sensitivity limits are 5σ limits. References: (a) GOODS *Spitzer* Legacy Program DR1, DR1+, and DR2; (b) Capak et al. (2004); (c) this work.
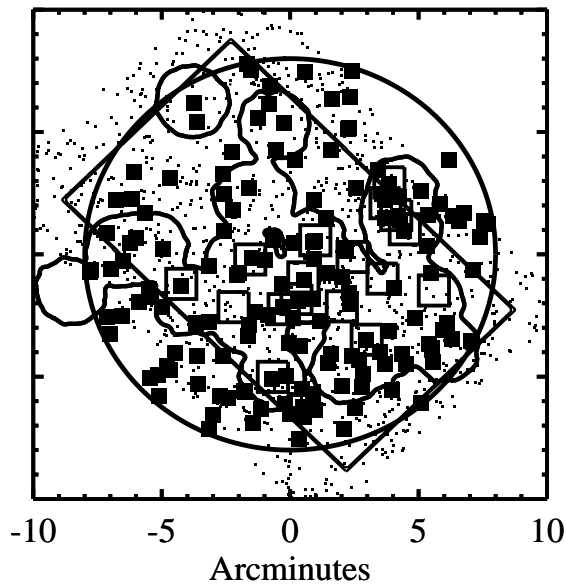

Fig. 1.— Schematic layout of the various images. The rectangle shows the deepest portion of the ACS GOODS-N image. The contours show the SCUBA image. The circle shows an $8'$ radius around the radio and X-ray centers. The large open squares denote the 17 SCUBA sources detected at the 4σ level, the solid squares denote the 20 cm sources within the $8'$ radius, and the dots denote the 24 μm sample. The total submillimeter area is 125 arcmin^2, and the area of overlap with the ACS GOODS-N rectangle, which we use as our primary area, is 106 arcmin^2. The ACS GOODS-N rectangle has an area of 144 arcmin^2.

with smaller solid squares, and the 24 μm sources with dots. Our core area excludes the more poorly sampled regions of the 24 μm image.

3. REDSHIFTS

3.1. *Spectroscopic Redshifts*

Intensive spectroscopic redshift surveys have been carried out in the ACS GOODS-N region. We searched for spectroscopic redshifts for the sources in Wirth et al.

(2004), Cowie et al. (2004), and Chapman et al. (2005). A substantial number of additional redshifts, which either lie outside the ACS GOODS-N region or were obtained from our spectroscopic runs with the Deep Extragalactic Imaging Multi-Object Spectrograph (DEIMOS; Faber et al. 2003) on the Keck 10 m telescope subsequent to the publication of these papers, were also included.

3.2. *Photometric Redshifts*

We used the U to 8 μm photometry of the sources to derive their photometric redshifts. We only considered sources that were detected in at least five bands. Compared to most optical photometric redshifts, adding the deep J and H magnitudes and the *Spitzer* data has the advantage of improving the high-redshift end of the photometric redshift determinations. The MIR photometry probes various spectral features, including the 1.6 μm bump caused by the opacity minimum in the stellar atmosphere and PAH emission at $5 - 9$ μm. In fact, the *Spitzer* photometry alone has been used to derive photometric redshifts based on the 1.6 μm bump (see e.g., Sawicki 2002; Egami et al. 2004).
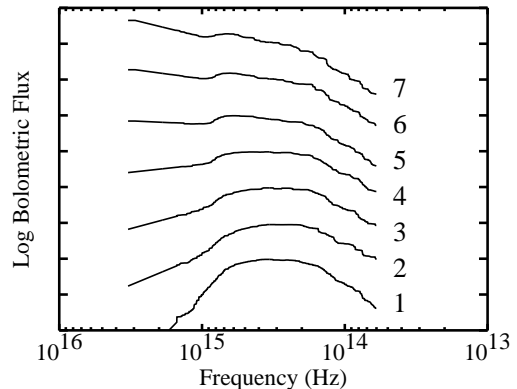

Fig. 2.— SED templates used in the training-set photometric redshift determinations. Vertical axes are arbitrarily scaled bolometric fluxes (νF_ν). The numerical labels give the SED classes, which range from class 1 (elliptical galaxies) to class 7 (very blue star-forming galaxies).

The primary difficulty of incorporating the MIR data into the photometric redshift estimation is the lack of optical to MIR galaxy spectrum templates. Pérez-González et al. (2005) overcame this problem by building "training-set" spectral energy distributions (SEDs) from the sources within the MIPS sample itself. We also used this method to generate our photometric redshifts. We used just over 1200 galaxies with known redshifts and spectral types in the ACS GOODS-N region to construct seven templates over the frequency range from 6×10^{13} Hz to 4×10^{15} Hz. These templates range from an elliptical galaxy spectrum to a very blue star-forming galaxy spectrum. The seven templates are shown in Figure 2. We then made a least-squares fit to these templates to determine the photometric redshifts and spectral types for the galaxies in each sample.

The method works extremely well over a wide range of redshifts and only fails for a small number of sources. In Figure 3, we compare our photometric redshifts with the spectroscopic redshifts for the spectroscopically-identified $H < 23$ sample in the ACS GOODS-N region. There are 1213 sources in this sample with spectroscopic

TABLE 2
PROPERTIES OF THE 850 μM SOURCES WITH 20 CM AND 24 μM MATCHES

ID	z_{sp}	z_{ph}	$S_{850\mu m}$ (mJy)	$S_{1.4GHz}$ (μJy)	$S_{3.6\mu m}$ (μJy)	$S_{24\mu m}$ (μJy)	$\mathrm{Log}(S_{HX})$ (ergs cm^{-2} s^{-1})
GOODS 850-3	1.865	2.71	7.7 ± 1.0	151	14.4	330	$\cdots$
GOODS 850-6	$\cdots$	2.17	13.6 ± 2.3	107	9.5	185	$\cdots$
GOODS 850-7	2.578	3.75	6.2 ± 1.0	53.9	9.8	313	-15.10
GOODS 850-9	2.490	2.31	7.1 ± 1.2	45.3	16.0	235	-15.04
GOODS 850-11	$\cdots$	2.67	10.8 ± 2.2	124	4.4	165	< -15.85
GOODS 850-15	$\cdots$	2.91	8.7 ± 2.0	148	13.4	370	$\cdots$
GOODS 850-16	$\cdots$	3.79	12.4 ± 2.9	324	15.4	267	$\cdots$
GOODS 850-17	1.013	1.22	5.7 ± 1.4	81.4	86.7	724	-14.65

redshifts that are not saturated in the optical ($z' > 19$), and 1134 of these have statistically acceptable fits to the templates at some redshift from $z = 0$ to 4. The remaining sources either have unusual SEDs or are blended with a neighbor. For the 1134 sources with both spectroscopic and photometric redshifts shown in Figure 3, there are only a couple of seriously discrepant sources, and while the scatter becomes larger at the higher redshifts, the method robustly places nearly all the sources in the correct redshift range.
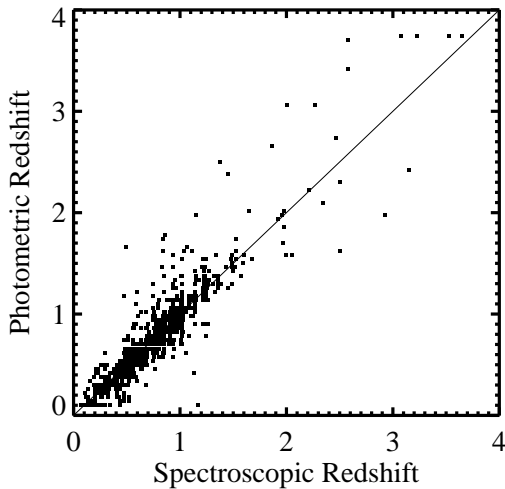

FIG. 3.— Comparison of our photometric redshifts, as determined from the training-set templates, with the spectroscopic redshifts for the spectroscopically-identified H-band sample in the ACS GOODS-N region.

4. IDENTIFICATION OF THE 850 MICRON EBL

4.1. *Direct Identification of Bright Submillimeter Sources*

Many of the bright (> 2 mJy) submillimeter sources that are directly detected in the 850 μm blank-field SCUBA images can be localized by their radio emission, as discussed in the introduction. However, since the 24 μm-band traces the short wavelength end of the FIR emission, the 24 μm sample may provide additional counterparts to the bright SCUBA sources (Egami et al. 2004; Ivison et al. 2004).

Our 850 μm SCUBA map covers 0.034 deg^2, and there are 17 4σ bright SCUBA sources in this area in the catalog of Wang, Cowie, & Barger (2004), whose notation

we shall follow. Three of the bright SCUBA sources (GOODS 850-2, 850-8, and 850-14) have no 24 μm counterparts, even within a very wide 8$''$ search radius. These sources also do not have radio counterparts (Wang, Cowie, & Barger 2004). The remaining 14 have a total of twelve 24 μm sources within a 6$''$ search radius and eighteen 24 μm sources within an 8$''$ search radius. Given the number density of 24 μm sources, we expect ~ 3 false matches at 6$''$ and ~ 5 false matches at 8$''$, so we are identifying some $9 - 13$ of the remaining 14 sources, or about $50 - 75\%$ of the total sample.

We can compare this with the counterpart identifications made using the 20 cm data by Wang, Cowie, & Barger (2004). Eight of the 17 4σ bright SCUBA sources have 20 cm counterparts within 6$''$, and we expect all of these to be real, given the surface density of radio sources. Ten have counterparts within 8$''$, including one source with two radio counterparts; we expect one false match at this radius. These results suggest that the 24 μm data may be slightly better at picking up the bright SCUBA sources, but the difference is not statistically significant. All eight radio sources with bright SCUBA counterparts within 6$''$ are seen at 24 μm, and the 24 μm data then picks out a further four sources, of which three are expected, on average, to be false.

The redshifts (spectroscopic and photometric) and properties of our eight securely identified bright SCUBA sources are summarized in Table 2. The whole 24 μm sample has a median 24 μm flux of 152 μJy. The SCUBA sources in Table 2 have a median 24 μm flux of 300 μJy and are weighted to the high end of the 24 μm fluxes. They are mostly at high redshifts ($z = 2 - 3$), with a median redshift of $z = 2.5$, and are consistent with being ULIRGs. Ivison et al. (2002) presented a sample of 30 radio-identified SCUBA sources with 850 μm fluxes > 8 mJy. Using the millimetric redshift technique, they found a median redshift of $z = 2.4$. Chapman et al. (2003a) presented a spectroscopic redshift sample of 10 radio-identified bright (> 2 mJy) SCUBA sources, and Chapman et al. (2005) expanded that sample to 73 sources. Their typical redshift range is $z = 1.7 - 2.8$, with a median redshift of $z = 2.2$. The redshift distribution of our radio-identified bright SCUBA sample is fully consistent with the results of the above groups.

4.2. *A Stacking Analysis of the Submillimeter EBL*

TABLE 3
850 μm Stacking Analyses

Waveband	Flux$_{min}$ (μJy)	N	Area (arcmin^2)	$< S_{850} >$ (mJy)	I_ν (Jy deg^{-2})	$I_{\nu,\mathrm{clean}}$ (Jy deg^{-2})
ACS 0.45 μm	0.05	6868	106	0.10 ± 0.017	$24.8(15.2) \pm 4.1(6.0)$	$14.3(19.3) \pm 4.0(6.0)$
ACS 0.8 μm	0.1	7826	106	0.10 ± 0.016	$26.8(16.3) \pm 4.3(6.4)$	$15.4(20.9) \pm 4.2(6.3)$
ULB 1.6 μm	1	3094	122	0.20 ± 0.03	$18.8(21.1) \pm 2.3(3.5)$	$10.4(17.7) \pm 2.3(3.5)$
IRAC 3.6 μm	0.3	5245	106	0.11 ± 0.0066	$19.6(16.7) \pm 3.4(5.1)$	$8.2(15.6) \pm 3.4(5.1)$
IRAC 8.0 μm	2.0	1587	106	0.33 ± 0.03	$18.0(19.0) \pm 1.9(2.8)$	$9.1(13.8) \pm 1.9(2.8)$
MIPS 24 μm	80	493	106	0.66 ± 0.06	$11.4(9.1) \pm 1.1(1.5)$	$5.9(5.6) \pm 1.1(1.6)$
VLA 20 cm	40	101	122	1.31 ± 0.13	$4.0(5.1) \pm 0.40(0.6)$	$1.5(2.7) \pm 0.4(0.6)$
NIR 1.6, 3.6 μm	1.8	3121	106	0.20 ± 0.025	$20.7(20.9) \pm 2.6(4.6)$	$11.4(16.1) \pm 2.6(4.0)$

Note. — The N values are the numbers of sources with errors less than 4 mJy that were used in the stacking analyses.

We cannot directly analyze the submillimeter sources that are too faint to be detected in blank-field SCUBA surveys, but we can use our galaxy samples at other wavelengths to study these sources using a stacking technique. This technique was first used by Peacock et al. (2000) to study the submillimeter properties of Lyman-break galaxies. Here we use our SCUBA map to determine the average 850 μm properties of the sources in a given sample, and hence the amount of 850 μm light they produce. Although such an analysis provides very little information on the individual source properties, it can show which of the galaxy populations give rise to the submillimeter light. Since we can also break the samples down by galaxy flux, color, spectral type, or redshift, we can determine the properties and redshift distribution of the class(es) of sources that is (are) producing the bulk of the 850 μm EBL.

One difficulty with trying to assess what fraction of the 850 μm EBL a class of sources produces is that the absolute normalization of the 850 μm EBL is somewhat uncertain. The observed 850 μm EBL is given as 31 Jy deg^{-2} in Puget et al. (1996) and as 44 Jy deg^{-2} in Fixsen et al. (1998). The substantial difference between the two estimates is a consequence of different corrections for foreground emission, and it is unclear which is the better estimate. We therefore compare with the full range in our subsequent analysis.

The possible source populations that are contributing the bulk of the 850 μm EBL are also constrained by the deepest submillimeter number counts. The 850 μm number counts of Cowie, Barger, & Kneib (2002) showed that the number of submillimeter sources with fluxes > 0.5 mJy is approximately 2.5×10^4 deg^{-2}. This is therefore a rough minimum on the density of any sample that seeks to explain the 850 μm EBL. Simply based on such number densities, it is clear that there are not enough 20 cm selected sources to account for the light, and there are only marginally enough 24 μm sources (approximately 1.8×10^4 deg^{-2} above 80 μJy). In other words, the current 20 cm and 24 μm samples are not deep enough to have reached the fainter submillimeter sources, while the NIR and MIR samples are deep enough to have surface densities that are substantially above the required value.

We first computed the contributions to the 850 μm EBL from seven samples: the H-band, 3.6 μm, 8 μm,

24 μm, and 20 cm selected samples, as well as the B and I-band selected samples from the ACS GOODS-N catalogs of Giavalisco et al. (2004). For each source in each sample, we determined the beam-weighted 850 μm flux and noise from our SCUBA map (see §2.1). We then measured the error-weighted average 850 μm flux for all of the sources in the sample that had errors less than the chosen cut value of 4 mJy. We also determined the area where each sample had submillimeter measurements of this sensitivity. The EBL contribution is then given by the product of the number of sources and their error-weighted mean divided by the observed area. The results are almost identical for cut values other than 4 mJy. The contribution of each population to the 850 μm EBL is summarized in Table 3, where we give the sample wavelength and limiting flux, the area covered, the number of sources, the error-weighted mean 850 μm flux for each source, the 850 μm EBL contribution with its 1σ error, and the 850 μm EBL contribution measured from a map where 4σ 850 μm sources are CLEANed (see below). Since the error weighting may result in a very small region dominating the signal, we also computed the unweighted 850 μm signal over the same area. This is given in parentheses in the final two columns of the table.

Our results confirm the MIR detections made by Serjeant et al. (2004) with the *Spitzer* Early Release Observations and the SCUBA 8 mJy survey, but at substantially higher significance levels. As an example, there are 493 24 μm sources with 850 μm errors less than 4 mJy in the SCUBA map. The mean 850 μm flux of these sources is 0.66 ± 0.06 mJy. This is a substantial improvement in signal to noise over the value of 0.30 ± 0.24 mJy found by Serjeant et al. (2004) due to the large number of 24 μm sources in the GOODS-N field. We obtain a consistent average flux of 0.53 ± 0.08 mJy from the unweighted sample, which shows that the lower error regions are not dominating the signal. The total stacking contribution of the 24 μm sources to the 850 μm EBL is 11.4 ± 1.1 Jy deg^{-2}, or about $25 - 35\%$ of the total 850 μm EBL.

As expected, given that they do not have sufficiently high number densities, the 20 cm and 24 μm samples only identify a fraction of the 850 μm EBL. (The radio sample identifies 4.0 ± 0.40 Jy deg^{-2}, or about $10 - 13\%$ of the 850 μm EBL.) It is clear that much deeper samples would be required at both of these wavelengths to sub-

stantially identify the 850 μm EBL. To try to see how much fainter we would have to go at 24 μm, we generated a fainter 24 μm source catalog using SExtractor and excluded the original 1173 MIPS sources. There are 731 3σ MIPS sources in this catalog, and 338 of them are in the SCUBA map. Their median 24 μm flux is 46 μJy, and the faintest ones are ~ 10 μJy. These faint 24 μm sources possess a weak 850 μm stacking signal of 1.73 ± 1.32 Jy deg^{-2}. We note that the completeness of the 24 μm catalog decreases rapidly from ~ 1.0 at 80 μJy to ~ 0.1 at 40 μJy (e.g., Papovich et al. 2004). Therefore, the faint 24 μm sources in the $10 - 80$ μJy range might make a significant contribution (> 10 Jy deg^{-2}) to the 850 μm EBL. However, because of the low statistical significance of the stacking signal, we cannot show that this is the case with the current data. To provide a definitive answer, we would need a substantially complete 24 μm catalog to about a 10 μJy flux.

By contrast, the 8 μm sample provides a much more substantial identification of the 850 μm EBL (18.0 ± 1.9 Jy deg^{-2}), as do all of the shorter wavelength bands. In fact, at first sight, the optical wavelength bands give the most complete identification of all. However, on closer inspection, much of this signal comes from the very small HDF-N region, where the submillimeter errors are very low. Here the slightly smaller EBL determined from the unweighted average may be a more representative value.

The signal from each of the samples is, of course, heavily overlapped, and we next compared the samples to see how much additional signal each added. To do this, we took each sample in turn as our primary sample and then measured signals from the residual sources in each of the other samples after each of the primary sample's overlapping sources were excluded. That is, we measured the signal from the other samples, after excluding all sources which were already present in the primary sample. We were able to determine which of the samples were most complementary based on this procedure. As a result of our analysis, we formed a sample from the combination of all sources with H-band or 3.6 μm fluxes greater than 1.8 μJy. We restricted the sample to the ACS GOODS-N region. We refer to this sample as our NIR sample, and we summarize its properties in the final line of Table 3. Physically, since the two bands bracket the peak flux in most galaxy SEDs over roughly the $z = 0 - 3$ range, this sample is choosing nearly all of the galaxies with peak observed fluxes above the 1.8 μJy cut.

From our NIR sample, we find a contribution of 20.7 ± 2.6 Jy deg^{-2}, or $50 - 70\%$ of the 850 μm EBL. Perhaps even more importantly, our NIR sample appears to contain nearly all of the EBL that can be measured from the remaining samples. In other words, when our NIR sample is excluded, none of the residual 8 μm, 24 μm, or radio sample sources gives a signal greater than 1 Jy deg^{-2}. The residual B and I-band sample sources give a signal of a few Jy deg^{-2} in the weighted samples but a null signal in the unweighted samples. We therefore adopt our NIR sample as our primary sample for further analysis.

There are 3121 sources in our NIR sample. Of these, 2415 are in the original $H < 24$ 3σ catalog, and a further 374 have H-band magnitudes brighter than 24, reflecting the incompleteness of this catalog in the $H = 23 - 24$ range. The remaining 332 sources in our NIR sample

would not have been selected in a complete $H = 24$ sample and have only been detected using the 3.6 μm catalog; they give a signal of 4.8 ± 0.9 Jy deg^{-2}. Thus, the combined catalog gives an improved identification of the EBL relative to either catalog alone.

We visually inspected the 3.6 μm image for all of the sources without optical or NIR counterparts to check that these were not spurious. About 30 sources are suspect, either because they are not clearly seen in the 3.6 μm image, or because they are contaminated by a neighbor. However, excluding these sources has no effect on the measured signal, and we conclude that there is a significant contribution from the 3.6 μm sources in the sample.

To check the robustness of our results, we performed a number of tests. First, we summed the total SCUBA image to find the total flux of our SCUBA map and found the result to be strictly zero. This is as expected, since each positive source in the SCUBA map has two negative 50% sidelobes. The zero sum of our SCUBA map indicates that there was good sky subtraction during the data reduction. Because of the zero sum of the submillimeter map, any random populations will have zero stacking fluxes, and a positive stacking signal will indicate a correlation between that population and the submillimeter sources. To test this and the assigned statistical errors, we measured fluxes for large numbers of random positions in the SCUBA image and analyzed these in the same fashion as the real samples. The results were fully consistent with expectations in both the average signal and the statistical spread.

The third test was a Monte Carlo simulation. We used the 24 μm source catalog and randomized its astrometry to create simulated 850 μm sources. The 850 μm fluxes of the simulated sources were derived from conversions based on M82 and Arp 220. The simulated sources were added into the "true noise" map of Wang, Cowie, & Barger (2004), which has both the bright SCUBA sources and the faint confusion sources removed, such that only noise is left. When we measured the 850 μm fluxes from the simulated maps, we randomly offset the measured positions from the source positions with up to $2''$ rms position errors, enough to account for the pointing errors of the submillimeter telescope and the astrometry errors in the 24 μm catalog. The average stacking flux was measured in 100 such realizations using the same methodology as was used in analyzing the true submillimeter image and fully recovered the known input fluxes. In summary, our Monte Carlo simulations and the zero sum of the SCUBA map show that the stacking flux is an unbiased estimate of the 850 μm EBL and that the assigned errors are realistic.

As our fourth test, we split the NIR sample into two parts: one corresponding to sources where the measured submillimeter errors lay between 0.1 and 1.5 mJy, and the other to sources where the errors lay between 1.5 and 4 mJy. The first sample contained 826 sources and gave an 850 μm EBL contribution of 20.1 ± 3.2 Jy deg^{-2}. The second sample contained 2295 sources and gave an 850 μm EBL contribution of 21.8 ± 4.5 Jy deg^{-2}, showing that an equivalent signal can be obtained from two samples with very different sensitivities.

Correlations in the target sample can result in an upward bias to the signal if the submillimeter flux comes

from overdense regions, since, in this case, we over-count the mean flux associated with each source (e.g., Serjeant et al. 2003). Given the expected angular correlations in the samples, we do not expect this effect to be large, but it may be present at some level. We tested this by measuring the average number of galaxies lying within 7" of a given galaxy. Since this is the half-width of the 850 μm beam, we expect that only galaxies within this area could be substantially contaminated. For the NIR sample described above, which has a surface density of 1.1×10^5 deg^{-2}, we found an average number of galaxies of 1.1 within this radius. This is actually smaller than the expected number for a random distribution (1.18), so there is very little correlated signal, and the correlation effects on the stacking signal are small. Since we shall subsequently restrict the sample even further, we ran this same test on that restricted sample and found a similar result.

Other groups (e.g., Serjeant et al. 2004) perform stacking analyses on maps where known submillimeter sources are removed. As our final test, we also removed all known submillimeter sources detected at or above the 4 σ level from the map and reran our stacking analyses. To do this we subtracted (CLEANed) the fitted PSFs of all of these sources from the image. Because our noise estimate does not include the confusion noise (e.g., Cowie et al. 2002; Wang et al. 2004), our 4 σ cut is comparable to the 3.5 σ cut used by most other groups. We note that such a sigma cut has different flux limits in different areas of our map. The totol flux removed from the map is only 5.6 Jy deg^{-2} but the sources removed from the deepest areas indeed correspond to a total surface brightness of $\sim$ 10 Jy deg^{-2} according to the number counts in Wang et al. (2004). The removal therefore affects the weighted contribution to the EBL more than the unweighted contribution and the later value is comparable to the reduction in the weighted signal while the former matches the change in the unweighted signal. As a consequence of this complex biasing effect from the non-uniform sensitivities, we decided to use only our un-CLEANed results. However, for completeness, we also include our CLEANed results in Table 3.

4.3. The 850 μm EBL versus Galaxy Flux, Color, and Spectral Type

We can further subdivide the contributions to the 850 μm EBL by galaxy flux, color, and spectral type to determine the properties of the sources giving rise to the light.

We show the contributions to the 850 μm EBL from the H-band sample versus the H-band flux in Figure 4 and from the 3.6 μm sample versus the 3.6 μm flux in Figure 5. In each case, we denote with solid squares the contributions in half dex flux intervals, starting at the limiting flux of the sample. The total contribution of the entire sample is given in the upper right corner. The individual source fluxes in mJy are denoted by dots; 4σ measurements are denoted by plus signs. For the lowest flux interval in the H-band sample, we also show the EBL value corrected for the incompleteness in the H-band catalog (open square). For both samples, the contributions are dropping at the faintest end, which would be consistent with the onset of convergence to the asymptotic value. The peak contribution comes near a flux of 6 μJy

in the H-band and near a flux of 18 μJy in the 3.6 μm-band. Expressed in magnitudes, the peak contribution to the measured signal is coming from sources with NIR magnitudes of $21 - 22$ (AB).
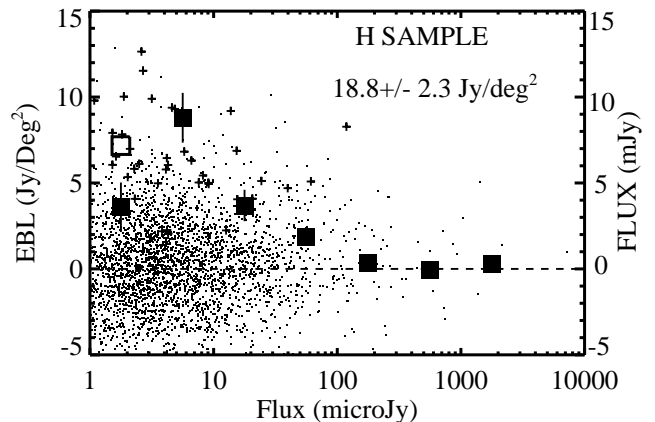

Fig. 4.— Contributions to the 850 μm EBL from the H-band sample vs. the H-band flux. The solid squares show the contributions from each half dex flux interval with 1σ error bars. The number in the upper right corner gives the total contribution. The open square shows the contribution from the lowest flux interval corrected for the incompleteness in the H-band catalog. The dots denote the measured fluxes of the individual sources for a y-axis in mJy units, and the plus signs denote sources with 4σ measurements at 850 μm.
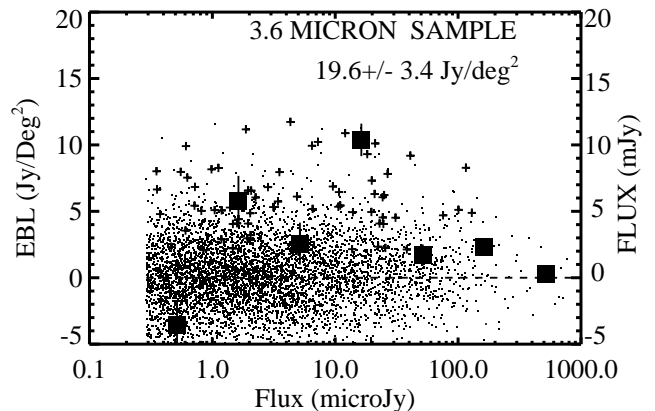

Fig. 5.— Contributions to the 850 μm EBL from the 3.6 μm sample vs. the 3.6 μm flux. The solid squares show the contributions from each half dex flux interval with 1σ error bars. The number in the upper right corner gives the total contribution. The dots denote the measured fluxes of the individual sources for a y-axis in mJy units, and the plus signs denote sources with 4σ measurements at 850 μm.

We show the contributions to the 850 μm EBL from the H-band sample versus the $I - H$ color in Figure 6 and from the 3.6 μm sample versus the $H - 3.6$ μm color in Figure 7. In both cases, the light comes from the redder sources in the sample. In the H-band sample, the $I - H$ color weighted by the submillimeter light contribution is 1.5, while the mean color of the whole sample is 1.0. This arises because there is a higher mean submillimeter signal per object (open diamonds) in the red-colored sources. Similarly, the 3.6 μm sample has a submillimeter-weighted color $H - 3.6$ μm of 1.2, as compared to a mean color of the whole sample
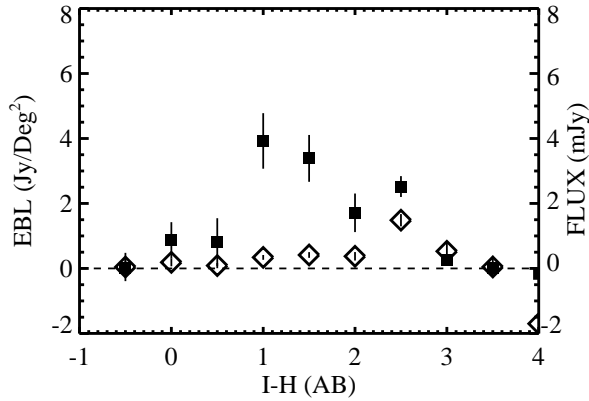
FIG. 6.— Contributions to the 850 μm EBL from the H-band sample vs. the $I - H$ color in AB magnitudes. The solid squares show the contributions from each color interval with 1σ error bars. The open diamonds show the mean 850 μm fluxes of the sources for a y-axis in mJy units.
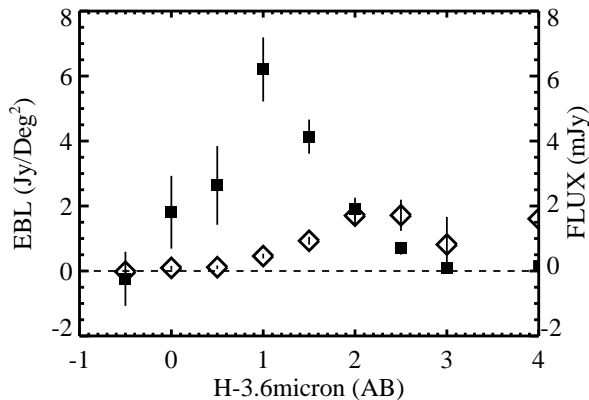

FIG. 7.— Contributions to the 850 μm EBL from the 3.6 μm sample vs. the $H - 3.6$ μm color in AB magnitudes. The solid squares show the contributions from each color interval with 1σ error bars. The open diamonds show the mean 850 μm fluxes of the sources for a y-axis in mJy units.

of -0.3. The cumulative signal in the H-band sample is 3.4 ± 1.1 Jy deg^{-2} for $I - H > 2$ and 14.5 ± 2.1 Jy deg^{-2} for $I - H > 1$.

This biased contribution of red galaxies to the submillimeter light is a known result from stacking analyses carried out using submillimeter measurements of extremely red objects in both lensed cluster and blank-field surveys (Wehner, Barger, & Kneib 2002; Webb et al. 2004; Knudsen et al. 2005).

However, the observed-frame colors are a function of galaxy type, reddening, and redshift, and we may make a much more powerful analysis using the photometric redshift determinations, which separately yield the redshift and the rest-frame SED for each source. In Figure 8, we show the 850 μm EBL contribution from the galaxies in the NIR sample divided into the seven SED classes used in our training-set photometric redshift analysis (see Fig. 2). We assign unidentified sources an SED class of zero, and we exclude spectroscopically-identified stars. The vertical lines split the sample into four bins: unidentified sources (class 0), elliptical galaxies (class 1), intermediate spiral galaxies (classes $2-5$), and very blue star-forming galaxies (classes 6 and 7). We have printed directly on the figure the number of sources in each of
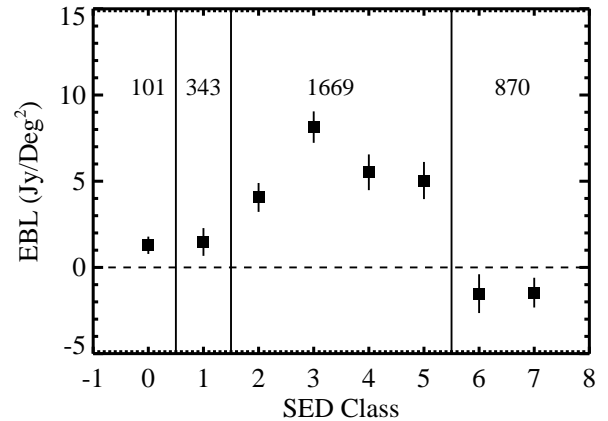
the four bins.

FIG. 8.— Contributions to the 850 μm EBL vs. the SED class. Unidentified sources are placed in class 0, and spectroscopically-identified stars are excluded. The solid squares show the contributions from each class with 1σ error bars. The vertical lines divide the sources into 4 bins, with the number of sources in each bin printed at the top of that bin.
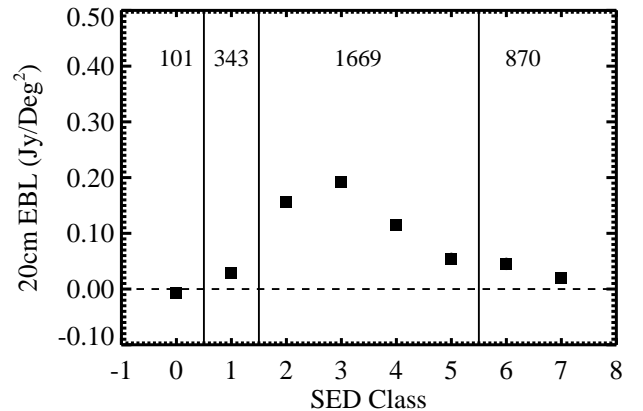

FIG. 9.— Contributions to the 20 cm EBL vs. the SED class. Unidentified sources are placed in class 0, and spectroscopically-identified stars are excluded. The solid squares show the contributions from each class with 1σ error bars. (These are smaller than the symbol size.) The vertical lines divide the sources into 4 bins, with the number of sources in each bin printed at the top of that bin.

Neither the elliptical galaxies nor the very blue star-forming galaxies give a significant signal. The 1213 galaxies in these three classes have an error-weighted 850 μm flux of -0.03 ± 0.04 Jy, presumably reflecting the lack of star formation in the elliptical galaxies and the absence of dust in the blue galaxies. Nearly all of the 850 μm signal comes from the intermediate spiral galaxies, which have an error-weighted 850 μm flux of 0.40 ± 0.03 Jy. There is a small contribution to the 850 μm EBL from the unidentified sources, which have an error-weighted 850 μm flux of 0.37 ± 0.14 Jy.

The same selection appears if we consider the 20 cm or 24 μm properties of the NIR sample as a function of SED class. In order to determine the average 20 cm flux of the NIR sample, we performed a stacking analysis using the 20 cm image of Richards (2000). (For the radio image, since the errors are constant, the average signal is the same as the error-weighted signal.) As with the submillimeter analysis, we measured the 20 cm fluxes for
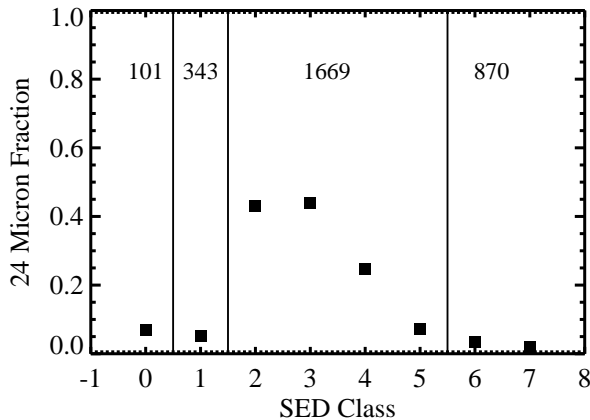
FIG. 10.— Fraction of the sources detected above a 24 μm flux of 80 μJy vs. the SED class. Unidentified sources are placed in class 0, and spectroscopically-identified stars are excluded. The vertical lines divide the sources into 4 bins, with the number of sources in each bin printed at the top of that bin.

FIG. 11.— Contributions to the 850 μm EBL from the unidentified (class 0) and intermediate spectral type (classes $2-5$) sources (i.e., our core NIR sample) vs. the greater of the H or 3.6 μm band fluxes. The solid squares show the contributions from half dex flux intervals with 1σ error bars. The number in the upper right corner gives the total contribution. The dots denote the measured fluxes of the individual sources for a y-axis in mJy units, and the crosses denote sources with 4σ measurements at 850 μm.

each of the sources in the NIR sample (see §2.6); the average 20 cm flux per source is 5.7 ± 0.34 μJy. In computing the 20 cm EBL, we eliminated the small number of 20 cm sources brighter than 300 μJy in the field, since none of these are directly detected submillimeter sources. The 20 cm EBL is dominated by the fainter sources, and this cutoff makes only a small change in the results. In Figure 9, we show the 20 cm EBL contribution from the galaxies in the NIR sample divided into the same seven SED classes. Here, too, nearly all of the radio light comes from the intermediate SED classes ($2 - 5$). These intermediate spiral galaxies have a signal of 9.1 ± 0.25 μJy.

In Figure 10, we show the fraction of sources in each SED class that are detected above 80 μJy at 24 μm based on the 24 μm catalog. Nearly all of the 24 μm sources with fluxes above 80 μJy also lie in the intermediate SED classes.

Given that the elliptical galaxies and the very blue star-forming galaxies are only a source of noise, we now remove these objects and the spectroscopically-identified stars from the NIR sample, leaving us with 1770 sources. We refer to this sample as our core NIR sample. The 850 μm EBL for these sources is plotted versus the greater of the H-band or 3.6 μm flux in Figure 11. The total contribution from this final sample is 24.0 ± 2.0 Jy deg^{-2}, or about $54-77\%$ of the total 850 μm EBL.

4.4. *The Redshift Distribution of the 850 μm EBL*

We may now use the photometric and spectroscopic redshifts to determine where in redshift space the 850 μm EBL arises. Nearly half of the sources (1478) in the full NIR sample have spectroscopic redshifts. Combining these with the photometric redshifts increases the identification to 3020. Only 101 sources are blended, too faint, or too peculiar in their SEDs to be identified.

In Figure 12, we show the 850 μm EBL that arises in the core NIR sample (that is, the intermediate SED classes plus the unidentified sources only) divided by redshift interval. Here the solid squares denote the contributions from the sample with either photometric or spectroscopic redshifts, and the open squares denote the contributions from the sample with spectroscopic red-
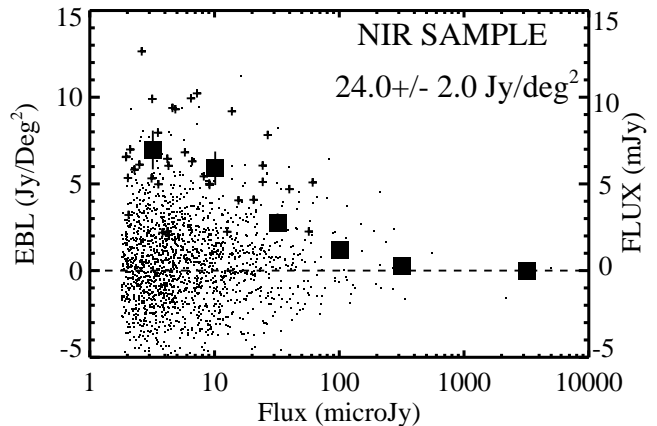
shifts only. Open diamonds show the average flux per source with a y-axis in mJy. The EBL from the core NIR sample is dominated by low-redshift sources. Indeed, 14.0 ± 1.6 Jy deg^{-2} of the EBL comes from below $z = 1.5$, implying that about half of the 850 μm EBL is originating at these low redshifts. This is in striking contrast to the redshift distribution of the bright SCUBA sources seen at higher fluxes and identified using their radio counterparts. It appears that at lower submillimeter fluxes, there is a substantial contribution to the 850 μm EBL from galaxies at much lower redshifts than is the case at the higher submillimeter fluxes.
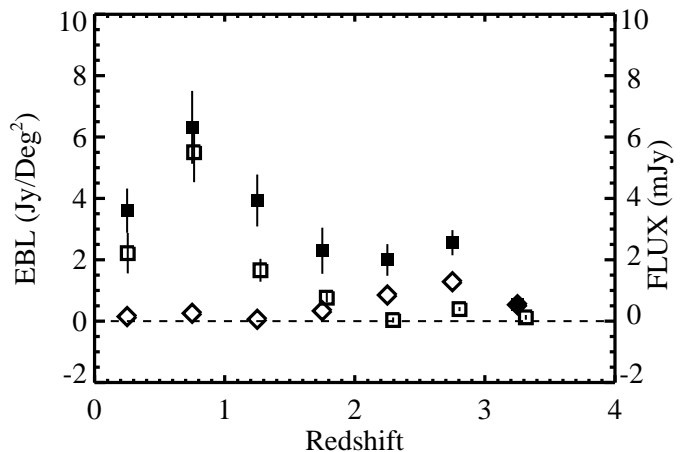

FIG. 12.— Contributions to the 850 μm EBL from our core NIR sample with spectroscopic or photometric redshifts vs. redshift. The solid squares show the contributions from each redshift interval with 1σ error bars. The open squares show the contributions if we only consider sources with spectroscopic redshifts. The open diamonds show the mean fluxes of the sources for a y-axis in mJy units.

5. THE STAR-FORMATION HISTORY

5.1. *The Star Formation Rate Density from the Core NIR Sample*

Subject to the assumed stellar mass function, the star-formation rates ($\dot{M}$ in $M_\odot$ yr^{-1}) of sources can be estimated from their infrared luminosities. In our analysis, we use the formula $\dot{M} = 1.7 \times 10^{-10} L_{\mathrm{IR}}/L_\odot$ (Kennicutt 1998). This is very similar to the value of $\dot{M} = 1.5 \times 10^{-10} L_{\mathrm{IR}}/L_\odot$ derived by Barger, Cowie, & Richards (2000).

The FIR luminosity can, in principle, be estimated from the $3.6 - 24$ μm flux, and this has been done to estimate the star-formation history of the 24 μm population. However, the conversion from $3.6 - 24$ μm flux to FIR luminosity is complex, so this method is relatively uncertain, and we do not follow it here.
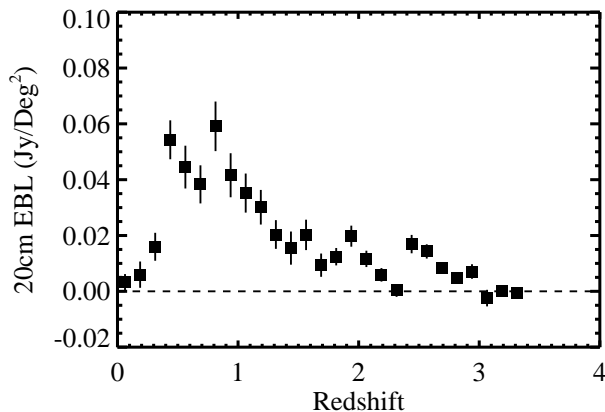

FIG. 13.— Contributions to the 20 cm EBL from our core NIR sample with spectroscopic or photometric redshifts vs. redshift. The solid squares show the contributions from each redshift interval with 1σ error bars.

The direct conversion of an 850 μm flux to a FIR luminosity is probably relatively robust for high-redshift ($z > 1$) ULIRGs, and we use this in §5.2 to estimate the star formation rate density (SFRD) for those sources. However, as we saw in §4.4, much of the submillimeter EBL that we have been able to identify from the core NIR sample is at lower redshifts, and the submillimeter flux to FIR luminosity conversion for these lower luminosity sources may have a much wider range. Thus, in order to compute the star-formation history of the core NIR sample, we use the 20 cm fluxes with their robust conversion of radio power to total luminosity.

In Figure 13, we show the 20 cm EBL versus redshift. We see a strong peak at a redshift of just below one, which then trails down to near zero beyond $z = 2.6$. We also generated the same plot for a large number of samples of randomized positions in the field containing the same number of sources. The random realizations average to zero, are fully consistent with the range expected from the statistical noise, and show no systematic effects. In addition, we computed the 20 cm EBL with redshift for only the sources in the Richards (2000) catalog with its limiting flux of 40 μJy. As might be expected, since this sample is considerably brighter in flux than the stacking sample, we found a lower peak redshift, with a value of $z \sim 0.5$.

We note that Figures 12 and 13 imply an unusually large submillimeter-to-radio flux ratio at $z \sim 1$. This is consistent with cool dust in local low-luminosity galaxies (e.g., Vlahakis, Dunne, & Eales 2005) or with a great amount of high-redshift background light being lensed by

low-redshift sources (e.g., Almaini et al. 2005).

We next translated the 20 cm EBL into a bolometric luminosity density for each redshift interval. We used the center redshift of the interval to compute the radio power per unit area, which we then converted to a total luminosity using the FIR-radio correlation (e.g., Condon 1992). We next computed the volume in each redshift bin for the unit area, thereby forming the total luminosity density per unit volume at that redshift.

In Figure 14, we show the SFRD of the core NIR sample obtained by converting the luminosity density to a SFRD using the Kennicutt (1998) relation. The SFRD (solid squares) shows a rapid rise to $z = 0.8$, and then it flattens at higher redshifts. Since some part of the light may arise from AGNs rather than star formation, we also show in Figure 14 the SFRD from only the sources that have X-ray luminosities less than 10^{42} ergs s^{-1} (open diamonds). This has only a small effect, so unless the correction for X-ray obscured AGNs is much larger, we can ignore the AGN contamination at our current level of accuracy.

At each redshift, the measured SFRD is a lower bound on the total submillimeter SFRD, since the core NIR sample is not a complete mapping of the submillimeter star-formation history. In particular, it may be biased to lower-redshift sources and preferentially miss the higher-redshift star formers. In §5.2, we assess the maximum corrections that are possible from the residual 850 μm light that the core NIR sample omits.

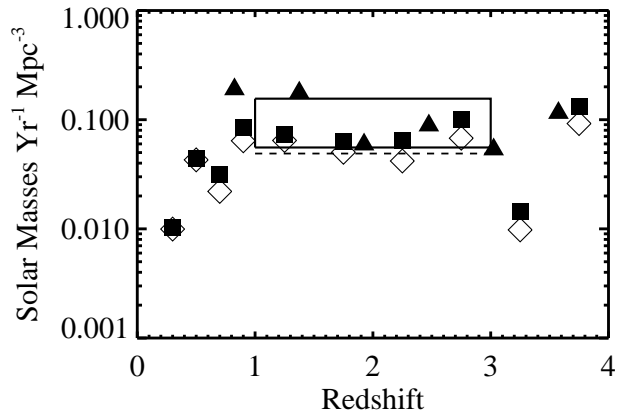

FIG. 14.— Submillimeter SFRD vs. redshift. The solid squares show the SFRD derived from the 20 cm EBL contributions of our core NIR sample. (The 1 σ errors are smaller than the symbol sizes.) The open diamonds show the same results when sources with a $2 - 8$ keV luminosity above 10^{42} ergs s^{-1} (sources containing AGNs) are excluded. The solid triangles show the SFRD computed using the 850 μm EBL. The dashed horizontal line shows the SFRD computed assuming all of the sources with 850 μm fluxes above 4 mJy lie at $z = 1 - 3$, as suggested by the bright source identifications. The rectangular region denotes the SFRD from the remaining submillimeter EBL that is not accounted for by our NIR sample, assuming that it also lies in the redshift interval $z = 1 - 3$. The range corresponds to the uncertainty in the 850 μm EBL. The maximum total submillimeter SFRD in this redshift range is then the sum of the rectangle and the measured points.

5.2. *Limits on the Star Formation Rate Density at*
$z = 1 - 3$

For the higher-redshift sources, where the galaxies are near-ULIRGs, we may make a direct estimate of the SFRD from the submillimeter light. We again assume that the luminosities are dominated by star formation. The infrared luminosities of the submillimeter sources can be estimated from their 850 μm fluxes, redshifts, a plausible dust temperature (T_d), and a dust emissivity index (β) in the submillimeter. To make this conversion, we adopted the dust model in Yun & Carilli (2002) and their values of $T_d = 58 \pm 9$ and $\beta = 1.32 \pm 0.17$ based on luminous and ultraluminous starbursts. This conversion is very similar to the one obtained for $T_d = 47$ and $\beta = 1.0$ (Arp 220), which has often been used in the past (e.g., Barger, Cowie, & Richards 2000).

We first computed the SFRD from the 850 μm EBL determined as a function of redshift for the core NIR sample. We computed the FIR luminosity per unit area in each redshift bin using the adopted dust model. Next, we computed the volume corresponding to the redshift interval. Finally, we converted the FIR luminosity per unit volume to a SFRD using the Kennicutt (1998) relation. The result is plotted in Figure 14 as the solid triangles. At $z > 1$, these results agree strikingly well with the 20 cm-determined SFRD shown by the solid squares. This is not a foregone conclusion, since we are using two independent data sets for the computation and two different (though hopefully consistent) calibrations for the conversion to luminosity. (The FIR-radio correlation in the case of the 20 cm conversion, and the Yun & Carilli (2002) dust model for the submillimeter conversion.) At $z < 1$, the 850 μm-determined SFRD is higher than the 20 cm determined SFRD, which is expected, since the adopted luminosity conversion may no longer be appropriate if the sources are no longer near-ULIRGs.

We next computed the SFRD assuming that all of the EBL from sources with 850 μm fluxes greater than 4 mJy is in the $z = 1 - 3$ range, where the identified sources of Table 1 lie. The fact that deep radio imaging only detects $\sim 60\%$ of the bright SCUBA sources suggests that the remaining 40% may be at redshifts greater than $z \sim 3$; thus, we may be overestimating this contribution. This result is plotted in Fig. 14 as the dashed line. The SFRD measured in this way is not independent of the SFRD measured in the core NIR sample, since the bright 850 μm sources may already be contained in the core NIR sample. Indeed, the directly determined value lies below the core NIR SFRD at these redshifts. This is because, while we are making the extreme assumption that all of the bright sources lie in this redshift range, only a small fraction of the 850 μm EBL lies at these bright fluxes (about 7 Jy deg^{-2}).

Finally, the maximum completeness correction for the submillimeter SFRD in this redshift interval can be determined from the residual 850 μm EBL that is not identified by the core NIR sample, assuming that it all lies at $z \sim 1 - 3$. Most likely only a part of this missing light will come from this redshift range and at least some may come from higher redshift sources where the counterparts at other wavelengths will be much fainter. This remaining light is approximately $7-21$ Jy deg^{-2} in 850 μm EBL, depending on the total EBL value used. The SFRD from the residual submillimeter EBL is shown by the rectangular area in Figure 14 and can be added to the SFRD from the core NIR sample to obtain the maximum pos-

sible submillimeter SFRD at each redshift.

The SFRD derived from the core NIR sample using the radio data is 0.09 $M_\odot$ yr^{-1} Mpc^{-3} at $z = 1$ and is almost identical to that at $z = 2 - 3$. Even the maximum completeness correction of 0.05 $M_\odot$ yr^{-1} Mpc^{-3} to 0.15 $M_\odot$ yr^{-1} Mpc^{-3} can only result in a star-formation history that is rising slowly above $z \sim 0.8$. When integrated through time, it appears that the majority of the star formation occurs around $z = 1$. Thus, previous claims that the submillimeter SFRD is strongly peaked at $z = 2 - 3$ appear to be incorrect.

5.3. Comparison with the UV-Determined Star Formation Rate Density

In Figure 15, we compare the SFRD determined here with the SFRD determined from UV observations. Both are computed consistently with a Salpeter IMF extending to 0.1 $M_\odot$. However, rather than plotting $\dot{\rho}$ versus redshift, as is usually done, we plot the quantity $\dot{\rho} \times t$ versus the cosmic time, t. The advantage of this display is that we can see more directly how many stars are formed at a given time. We use diamonds and triangles to show the direct star formation determinations from the UV light without any correction for extinction. We use solid squares to show our directly measured FIR star formation, and we use open squares to show our maximal corrections for the missing EBL, if it is formed in the $z = 1 - 3$ redshift range.

The FIR star formation is about a factor of 3 to 5 higher than the uncorrected UV star formation, depending on the correction applied for the missing 850 μm light *(dotted curves)*. The lower value corresponds to the directly measured light, and the upper value to the maximally corrected light. This is consistent with the usual dust corrections applied to the UV star formation rates, but it should be noted that the samples are somewhat disjoint, in that the blue star-forming galaxies (our template classes 6 and 7) contribute substantially to the UV star formation but not to the FIR star formation. Thus, the extinction corrections must be higher in the galaxies that produce the bulk of the FIR light and lower in the blue star-forming galaxies.

We have also computed the total amount of stars formed as a function of time by combining the FIR and UV star-formation histories and integrating with respect to cosmic time. Above $z = 4$, where we do not have any information about the FIR light, we have assumed that the total star formation is five times the UV star formation, but the results at later times are quite insensitive to this assumption, since only a very small part of the total star formation occurs at these early times. The cumulative total is shown by the solid curves, where the lower curve corresponds to the directly measured FIR star formation and the upper curve to the maximally corrected FIR star formation. At $z = 0$, the curves match suprisingly well to the local determination of the stellar mass density (Cole et al. 2001), which is shown by the large solid circle in Figure 15. The agreement is best for the lower estimates, but even for the maximally corrected case, the curve is only slightly high. For the directly measured case, half of the star formation occurs at $z < 1.3$, while in the maximally corrected case, this rises to $z < 1.45$.
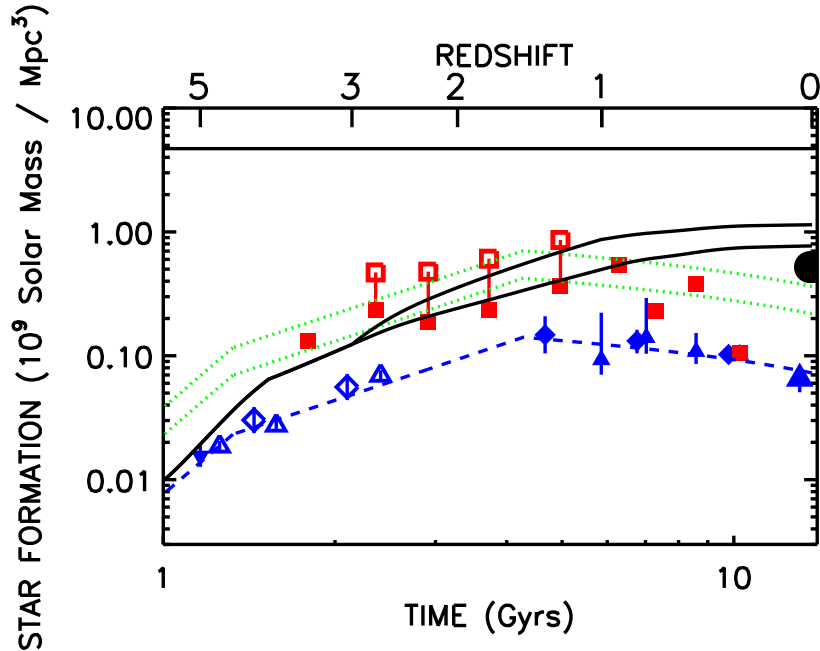
FIG. 15.— Comparison of the star formation history vs. cosmic time from our FIR determinations with that from UV samples. We plot the star formation rate density computed for a Salpeter IMF extending to 0.1 $M_\odot$ multiplied by the cosmic time, since this shows more clearly what fraction of the baryonic mass in stars is created at any time. The triangles and diamonds show the star formation that is directly seen at rest-frame UV wavelengths. At late times, we show the local *Galaxy Evolution Explorer* (GALEX) determination of Wyder et al. (2005) *(large solid triangle)*, the GALEX determinations of Schiminovich et al. (2005) *(small solid triangles)*, and the ground-based determinations of Wilson et al. (2002) *(small solid diamonds)*, which are the most accurate measurements near $z = 1$. At intermediate times, we show the determinations of Steidel et al. (1999) *(open diamonds)*, Bouwens, Broadhurst, & Illingworth (2003) *(small open triangles)*, and Iwata et al. (2003) *(solid upside-down triangle)*. The dashed curves show a parameterized fit. The dotted green curves show the total star formation that would be inferred if we were to apply reasonable extinction corrections to the UV light (upper curve = 5, lower curve =3). The solid red squares show this paper's FIR determinations, and the open red squares show our maximal corrections for incompleteness in the $z = 1 - 3$ range. There is broad agreement of the FIR determinations with the dust-corrected UV determinations, though the populations giving rise to the FIR light are somewhat disjoint from those giving rise to the UV light. The horizontal line shows the cosmic baryon density. The solid curves show the cumulative star formation. The solid black circle shows the present-day stellar baryon density estimated by Cole et al. (2001).

6. SUMMARY

We have obtained accurate redshifts for the sources in the GOODS-N area using existing spectroscopic redshifts and improved photometric redshifts from NIR and MIR data. The radio-identified bright (> 2 mJy) SCUBA sources in this area are in the redshift range $z \sim 1 - 3$ and have a median redshift of $z = 2.5$, consistent with previous radio and spectroscopic surveys.

However, we used a stacking analysis to show that much of the 850 μm EBL is in fact traced by a NIR sample constructed from sources with fluxes greater than 1.8 μJy in either the H or 3.6 μm bands. We showed that much of this light arises from galaxies with intermediate spectral types at $z < 1.5$. Thus, many of the fainter submillimeter sources that give rise to most of the 850 μm EBL are at lower redshifts and lower luminosities than the bright submillimeter sources that are detected directly.

Finally, we used a stacking analysis to estimate the average 20 cm EBL produced by the unidentified or intermediate spectral type galaxies in our NIR sample as a function of redshift, from which we determined the SFRD. We found that this SFRD evolves rapidly between $z = 0$ and $z = 0.8$, after which it becomes approximately flat. Using the submillimeter data directly, we then calculated a submillimeter based SFRD at $z \sim 1 - 3$ which agrees closely with the radio based SFRD. In addition, by assuming that all of the submillimeter EBL that is not accounted for by our NIR sample is also at these redshifts, we put an upper bound on the SFRD at $z \sim 1-3$. Even with this maximum completeness correction, we found consistency with a nearly flat or slowly rising extrapolation of the SFRD from $z \sim 1$. We conclude that the majority of the star formation traced by the submillimeter light comes from redshifts near one rather than at the higher redshifts that have been favored until now.

REFERENCES

Almaini, O., Dunlop, J. S., Willott, C. J., Alexander, D. M., Bauer, F. E., & Liu, C. T. 2005, MNRAS, 358, 875

Alexander, D. M. et al. 2003, AJ, 126, 539

Barger, A. J. et al. 1998, Nature, 394, 248

Barger, A. J., Cowie, L. L., & Sanders, D. B. 1999a, ApJ, 518, L5

Barger, A. J., Cowie, L. L., Smail, I., Ivison, R. J., Blain, A. W., & Kneib, J.-P. 1999b, AJ, 117, 2656

Barger, A. J., Cowie, L. L., & Richards, E. A. 2000, AJ, 119, 2092

Bennett, C. L. 2003, ApJS, 148, 1

Bertin, E. & Arnouts, S. 1996, A&AS, 117, 393

Bertoldi, F. et al. 2000, A&A, 360, 92

Borys, C., Chapman, S., Halpern, M., & Scott, D. 2003, MNRAS, 344, 385

Borys, C., Scott, D., Chapman, S., Halpern, M., Nandra, K., & Pope, A. 2004, MNRAS, 355, 485

Bouwens, R., Broadhurst, T., & Illingworth, G. 2003, ApJ, 593, 640

Capak, P. et al. 2004, AJ, 127, 180

Carilli, C. L. & Yun, M. S. 1999, ApJ, 513, L13

Chapman, S. C., Scott, D., Borys, C., & Fahlman, G. G. 2002, MNRAS, 330, 92

Chapman, S. C., Blain, A. W., Ivison, R. J., & Smail, I. R. 2003a, Nature, 422, 695

Chapman, S. C., et al. 2003b, ApJ, 585, 57

Chapman, S. C., Blain, A. W., Smail, I., & Ivison, R. J. 2005, ApJ, 622, 772

Chary, R. et al. 2004, ApJS, 154, 80

Chary, R. et al. 2006, in preparation

Cole, S., et al. 2001, MNRAS, 326, 255

Condon, J. J. 1992, ARA&A, 30, 575

Cowie, L. L., Barger, A. J., & Kneib, J.-P. 2002, AJ, 123, 2197

Cowie, L. L., Barger, A. J., Hu, E. M., Capak, P., & Songaila, A. 2004, AJ, 127, 3137

Dickinson, M. et al. 2006, in preparation

Eales, S., Lilly, S., Gear, W., Dunne, L., Bond, J. R., Hammer, F., Fèvre, O. L., & Crampton, D. 1999, ApJ, 515, 518

Eales, S., Lilly, S., Webb, T., Dunne, L., Gear, W., Clements, D., & Yun, M. 2000,

Eales, S., Bertoldi, F., Ivison, R., Carilli, C., Dunne, L., & Owen, F. 2003, MNRAS, 344, 169

Egami, E. et al. 2004, ApJS, 154, 130

Fazio, G. G. et al. 2004, ApJS, 154, 10

Faber, S. M. et al. 2003, Proc. SPIE, 4841, 1657

Fixsen, D. J., Dwek, E., Mather, J. C., Bennett, C. L., & Shafer, R. A. 1998,

Giavalisco, M. et al. 2004, ApJ, 600, 93

Huang, J.-S. et al. 2004, ApJS, 154, 44

Hughes, D. H. et al. 1998, Nature, 394, 241

Hughes, D. H. et al. 2002, MNRAS, 335, 871

Ivison, R. J., Smail, I., Barger, A. J., Kneib, J.-P., Blain, A. W., Owen, F. N., Kerr, T. H., & Cowie, L. L. 2000, MNRAS, 315, 209

Ivison, R. J. et al. 2002, MNRAS, 337, 1

Ivison, R. J. et al. 2004, ApJS, 154, 124

Iwata, I., et al. 2003, PASJ, 55, 415

Kennicutt, R. C. 1998, ARA&A, 36, 189

Knudsen, K. K., et al. 2005, ApJ, 632, 9

Loose, M., Farris, M. C., Garnett, J. D., Hall, D. N. B., & Kozlowski, L. J. 2003, Proc. SPIE, 4850, 867

Monet, D. G. et al. 2003, AJ, 125, 984

Papovich, C. et al. 2004, ApJS, 154, 70

Peacock, J. A. et al. 2000, MNRAS, 318, 535

Pérez-González, P. G. et al. 2005, ApJ, 630, 82 (P05)

Puget, J.-L., Abergel, A., Bernard, J.-P., Boulanger, F., Burton, W. B., Desert, F.-X., & Hartmann, D. 1996, A&A, 308, L5

Richards, E. A. 2000, ApJ, 533, 611

Rieke, G. et al. 2004, ApJS, 154, 25

Sanders, D. B. & Mirabel, I. F. 1996, ARA&A, 34, 749

Schiminovich, D., et al. 2005, ApJ, 619, L47

Sawicki, M. 2002, AJ, 124, 3050

Scott, S. E. et al. 2002, MNRAS, 331, 817

Serjeant, S. et al. 2003, MNRAS, 344,887

Serjeant, S. et al. 2004, ApJS, 154, 118

Smail, I, Ivison, R. J., & Blain, A. W. 1997, ApJ, 490, L5

Steidel, C. C., Adelberger, K. L., Giavalisco, M., Dickinson, M., & Pettini, M. 1999, ApJ, 518, 1

Trouille, L. et al. 2006, in preparation

Vlahakis, C., Dunne, L., & Eales S. 2005, MNRAS, 364, 1253

Wang, W.-H., Cowie, L. L. & Barger, A. J. 2004, ApJ, 613, 655

Webb, T. M. et al. 2003, ApJ, 587, 41

Webb, T. M. et al. 2004, ApJ, 605, 645

Wehner, E. H., Barger, A.J., & Kneib, J.-P. 2002, ApJ, 577, L83

Wilson, G., Cowie, L. L., Barger, A. J., & Burke, D. J. 2002, AJ, 124, 1258

Wirth, G. D. et al. 2004, AJ, 127, 3121

Wyder, T. K., et al. 2005, ApJ, 619, L15

Yun, M. S. & Carilli, C. L. 2002, ApJ, 568, 88